ACS Catalysis

pubs.acs.org/acscatalysis Research Article

Ligand-Field Directed Electronic Effects in Heterogenized Bifunctional Co(II) Molecular Clusters Accomplish Efficient Overall Water Splitting

Aditya Borah, Jayeeta Saha,[†] Sunita Sharma,[†] Savi Chaudhary, Sandeep K. Gupta, Gopalan Rajaraman,* Chandramouli Subramaniam,* and Ramaswamy Murugavel*

Cite This: *ACS Catal.* 2023, 13, 8535−8550 Read Online

ACCESS | Metrics & More | Article Recommendations | Supporting Information

ABSTRACT: We demonstrate a hitherto unknown approach of employing cobalt organophosphate D4R cage-clusters, $[(RO)PO_3Co(L)]_4$ (**1**−**4**) and $[nBu_4N][F@\{(RO)PO_3Co(L)\}_4]$, (**1F**−**4F**), where L = DMSO (**1** or **1F**), pyridine (**2** or **2F**), 4-formylpyridine (**3** or **3F**), and 4-cyanopyridine (**4** or **4F**), as bifunctional heterogeneous catalysts for electrochemical water splitting in near-neutral conditions. Electronic and steric modifications on the clusters are achieved through a synergistic combination of endohedral trapping of fluoride ion and exohedral functionalization of pyridines. This two-pronged approach significantly reduces the charge density at the metal leading to energetically favorable water coordination with a perceptible enhancement in the kinetics of overall water splitting, with **4F** exhibiting the lowest cell overpotential of 0.949 V (overall cell potential 2.179 V), observed among molecular catalysts. Density functional calculations highlight the importance of cooperativity between the cobalt centers. The unique D4R geometry stabilizes the high-valent metal-oxo/hydroperoxo species, emphasizing the need for polynuclear clusters to catalyze such challenging reactions, as has been well-established in the evolutionary PS-II.

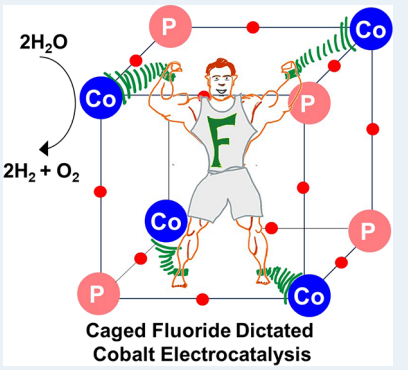

KEYWORDS: *bifunctional catalysts, molecular catalysis, overall water-splitting, geometry-driven cooperativity, ligand field design, DFT calculations, cobalt phosphates*

INTRODUCTION

Earth-abundant, heterogeneous electrocatalysts for energy-efficient water splitting has been the holy grail for realizing a hydrogen-driven economy.[1−19] Various design approaches such as doping, nanostructuring, and strain-engineering have been adopted for developing electrocatalysts that function close to the thermodynamic value.[20−27] Interface-driven heterogeneous electrocatalysts for water splitting have been predominantly based on transition metal-based nanosystems and their variants for achieving energy-efficient kinetic enhancements.[28−31] Among the systems that have been investigated, Co-based molecular systems and extended solid-state materials occupy a considerable space owing to the unique multivalent redox properties associated with the Co-center, as has been exemplified by the initial report on the Co(II)-phosphoric acid system in aqueous alkaline conditions.[20,32−35] Since then, well-defined, atom-precise Co-based clusters (either as Co(II)/Co(III)) are being extensively explored to not only glean mechanistic aspects of water splitting but also to improve the overall energy-efficiency.[36−38] In this direction, a cubane-like $[Co(III)_4O_4]$ cluster (a clone inspired by photosystem Mn_4Ca cluster) has been a promising candidate for unravelling the molecular pathways leading to water splitting.[39−44] The use of well-defined atom-precise molecular Co systems, stabilized by appropriate ligand fields, have been largely inaccessible due to the lack of design approaches and inability to prevent aggregation during catalysis. Interestingly, there have not been any significant attempts to investigate Co(II) based molecular systems for this purpose, especially those built from phosphate-based ligands, despite the fact that Co(II) state has been established as a key state through both theoretical and experimental mechanistic investigations.[3,45]

Our interest in this area stems from our earlier observations that Co(II) centers can easily be stabilized by phosphoric acid diesters, leading to both discrete or polymeric organic-soluble and water insoluble materials.[46−48] Subsequent investigations on these Co(II) based systems by us and Tilley et al. have indeed established that these thermo-labile systems can be

Received: December 2, 2022
Revised: May 15, 2023
Published: June 13, 2023

https://doi.org/10.1021/acscatal.2c05942
ACS Catal. 2023, 13, 8535−8550

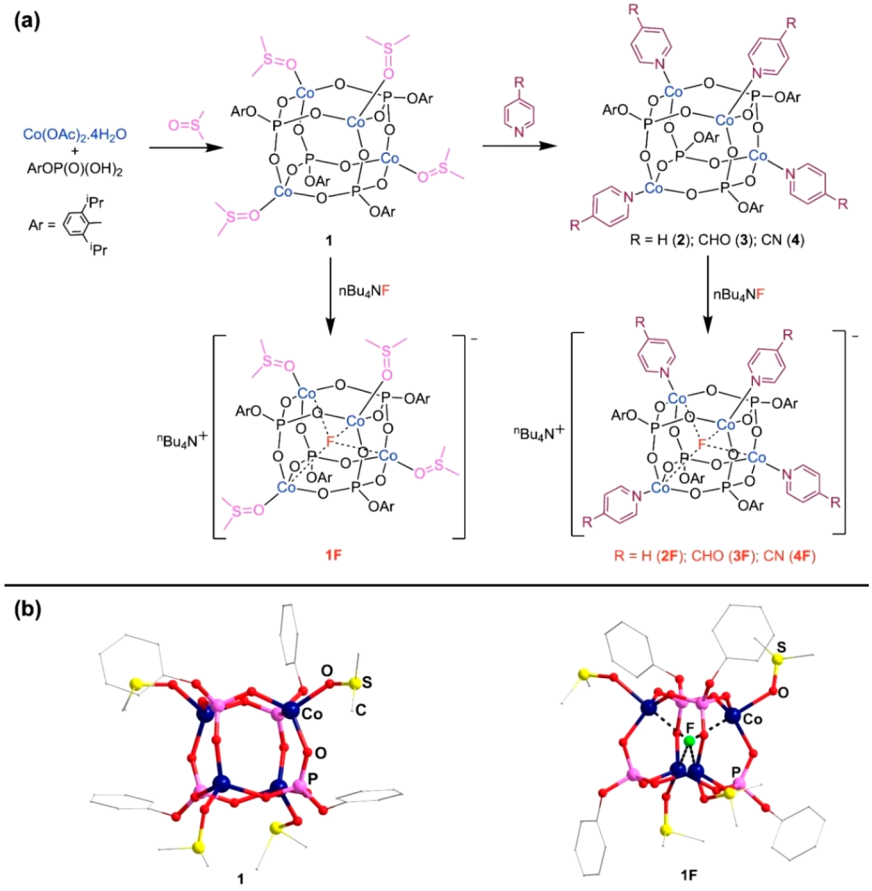

Figure 1. (a) Synthetic strategy employed for preparing cobalt phosphate clusters **1**−**4** and **1F**−**4F**. (b) Molecular structures of **1** and anionic part of **1F** as representative example. H atoms and isopropyl groups of phenyl rings are omitted for clarity.

transformed into useful electrocatalysts either in their pristine or immobilized states using suitable hosts.[3,49] These dialkyl phosphates however are not amenable for their use in molecular/cluster catalysis owing to the fact that they are both thermally unstable and lack functional diversities which can be used to fine-tune the electronic effects that lead to superior catalytic efficiencies. Hence, it becomes important to design ligands that can embrace more metal ions leading to the preferential formation of clusters, rather than solid-state materials. Thus, in a renewed attempt to achieve this synergism in synthesis for driving the desired electronic effects, we have switched over to a phosphoric acid monoester whose metal harvesting pocket is PO_3^{2-}, rather than the earlier diesteric PO_2^- units. Indeed this strategy was extremely successful in assembling molecular clusters that resemble zeolitic D4R, D6R and D8R units incorporating a range of redox active metal centers.[50−55] In this direction, we have recently shown that a cubane shaped D4R Co cluster can be assembled using a simple neutralization reaction between cobalt acetate and 2,6-diisopropylphenylphosphate under ambient conditions.[56] The structural resemblance of these Co(II) phosphate clusters to the Mn_4Ca photosystem[57] warranted a systematic investigation into their electrocatalytic water splitting behavior both in their pristine and electronically enhanced variations. In order to achieve the latter objective, we have relied on incorporation of fluoride anion inside the D4R cubane[58] with concurrent exocubane ligand-driven modulation of charge-density on the Co(II) center. The results of these investigations leading to exceptional kinetic enhancement to HER, OER and overall water splitting, with activities rivalling traditional Pt/IrO_2 catalysts, are presented in this communication.

RESULTS AND DISCUSSION

Design Principles. Formation of cubane-like clusters essentially make use of corner sharing tetrahedral ions of the type EO_4^{n-} as has been established in zeolite science.[59] While SiO_4^{4-} ions, along with sporadically substituted with Al^{3+} ions, have been the essential building blocks for the Bronsted acidic zeolites, much of the more-recent hydrophobic neutral aluminophosphates (AlPOs) chemistry originates from PO_4^{3-} and Al^{3+} ions.[60] Pruning the dimensionality of the phosphate-based extended solids to discrete entities would warrant suitable modification of the phosphoric acid to its dianionic $(RO)PO_3^{2-}$ form rather than the original trianionic form.[45,61] This not only restricts the growth of the structures in the third dimension, but also paves the way for incorporation of divalent cationic centers such as Co(II), instead of Al(III). This strategy has been a mainstay in our design principles to introduce the entire first row transition metals in their divalent form into a cubane-like architecture that resembles the D4R building block. Importantly, the high propensity for Co(II) ions to adopt a tetrahedral geometry over other coordination polyhedra enables realization and isolation of a range of tetrahedral Co(II) tetranuclear clusters.[56] An added advantage of using such systems stems from the fact that the electronic state of Co(II) metal centers can be precisely engineered through a two-pronged approach consisting of: (a) incorporation of a highly electronegative F^- ion which acts as a charge

https://doi.org/10.1021/acscatal.2c05942
ACS Catal. 2023, 13, 8535−8550

sink and (b) introduction of an exocubane ligand at each Co(II) center which can be substituted with either an electron-donating (e.g., $-NH_2$) or -withdrawing para-substituent (e.g., −CN) on the donor pyridinic ring. Figure 1a summarizes these design principles employed in the present study.

Synthesis and Structures of the Clusters. An equimolar reaction between the monoaryl phosphate, $(RO)PO_3H_2$ (R = 2,6-diisopropylphenyl) and cobalt(II) acetate in DMSO under ambient conditions yields $[(RO)PO_3Co(DMSO)]_4$ (**1**) as single crystals directly from the reaction mixture (Figure 1). Addition of more Lewis basic pyridines to the above reaction mixture results in replacement of DMSO by the corresponding pyridinic ligands to yield $[(RO)PO_3Co(L)]_4$ (L = pyridine (**2**), 4-formylpyridine (**3**) and 4-cyanopyridine (**4**)). These D4R shaped clusters **1**−**4** further react with tetrabutylammonium fluoride, once again under ambient conditions, resulting in the formation of fluoride-incorporated cubane clusters $[^nBu_4N][F@\{(RO)PO_3Co(L)\}_4]$ (L = DMSO (**1F**), pyridine (**2F**), 4-formylpyridine (**3F**) and 4-cyanopyridine (**4F**)), respectively. The pristine and fluoride incorporated clusters **1**−**4** and **1F**−**4F** have been extensively characterized through analytical and spectroscopic techniques. Raman spectroscopy, in particular, provides clear evidence of the symmetry breaking in **1F**−**4F**, as compared to **1**−**4**. Characteristic peaks at 560 cm^{-1} (Co−O, F_{2g}) and 460 cm^{-1} (Co−O, E_{1g}) and 699 cm^{-1} (P−O) and 1020 cm^{-1} (pyridine, **2**−**4** and **2F**−**4F**) are observed for all the cubanes (**1**−**4** and **1F**−**4F**). In addition, a prominent Co−F vibrational mode (420−440 cm^{-1}) is observed for **1F**−**4F**. Interestingly, the strength of this Co−F vibrational mode varies with the inductive effect of the distal, exocubane functional group, with a red-shift observed for **4F** compared to **1F**, indicating the more polarized Co−F bond (Figure S2).

The molecular structures of both pristine and fluoride incorporated clusters have been unambiguously established through single crystal X-ray structure determination of **1**, **2**, **3**, **1F**, **2F**, **3F**, and **4F**. The structures of **3** and **3F** have been established as the hemiacetal forms rather than the original aldehydic forms in view of the fact that the diffraction quality single crystals could be obtained only in methanol. While the molecular structures of **1** and **1F** are shown in Figure 1b, the details of other molecular structures and key bond parameters are elaborated in the ESI (Figure S3−S9). It can be seen that the pristine clusters (**1**, **2**, and **3**) have close structural resemblance to the zeolitic D4R SBU, whose central $Co_4P_4O_{12}$ core is a face-to-face dimer of two single-4-crowns. The bulky aryloxides on the phosphorus along with the pyridinic ligands on the cobalt offer an organic envelope for the inorganic core. This protective coating ensures stabilization of cobalt(II) centers. The way in which the eight heavy atoms and 12 oxygen centers are arranged in the cluster leaves sufficient void inside the cubane for incorporation of lighter anions. Such anion inclusion in the case of $(PhSi)_8O_{12}$ silasesquioxane clusters have been previously observed when their synthesis was achieved through hydrolysis of silyl esters in the presence of an anionic source.[62] The fact that the $Co_4P_4O_{12}$ is far less covalent than a Si_8O_{12} core offers opportunities to introduce an anion inside the core post assembly of the clusters. Thus, the compounds **1F**−**4F** derived by such postsynthetic anion inclusion of clusters **1**−**4** house fluoride anions at the center of the cubane as depicted in the molecular structure of **1F** in Figure 1b, as a representative example.

This inclusion of fluoride anion inside the cubane brings about significant structural distortions on the shape of the cluster as well as the coordination geometry of the metal ion. For example, the tendency of the fluoride ion to simultaneously interact with all the four Co(II) ions, results in their inward movement toward the central fluoride ion accompanied by an outward movement of the phosphorus centers. These movements of heavy atoms also have a bearing on the position of the oxygen centers. As a result, the local symmetry around the L-CoO_3 unit in **1**−**4** changes from an apparent C_{3v} symmetry to a pseudo-D_{3h} symmetry for the F@LCoO_3 units in **1F**−**4F**, a structural transformation pictorially represented in Figure 2 for the conversion of **1** to **1F** by the

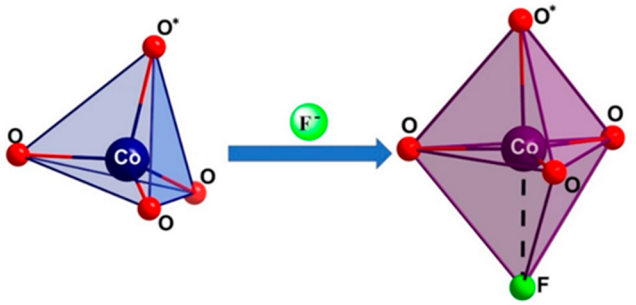

Figure 2. Effect of fluoride ion incorporation at the center of cubane **1** to produce **1F**. O* is the O atom of DMSO and other three oxygens are from phosphate. Only one of the four Co-centers of the D4R cluster is depicted as a representative case.

endohedral addition of fluoride ion. In **1**, the three Co−O(P) bonds around each cobalt exhibit an average bond length of 1.915 Å. On fluoride encapsulation, these bonds elongate to 1.951 Å, an effective average elongation of 36 pm for each bond. Interestingly, the fluoride incorporation also elongates the exocubane Co−O(DMSO) bond from 2.007 to 2.110 Å, with a net lengthening of 113 pm. Thus, the Co−O bond trans to fluoride is significantly elongated compared to those equatorial Co−O bonds (cis to fluoride). This lengthening is quite significant in spite of the fact that the fluoride ion is only weakly interacting and almost equidistant to the four cobalt ions (average Co−F = 2.316 Å). Similar elongations have also been observed for **2F**−**4F**. Concurrently, the tetrahedral O−Co−O angles in **1** are transformed to cis and trans trigonal bipyramidal (tbp) angles of 120°, 90°, and 180° in **1F**, respectively (see ESI, Table S11 and S12).

To investigate the type of magnetic interactions among the Co(II) centers in pristine and fluorinated clusters, the temperature dependence of magnetization ($\chi_M T$ vs T) has been explored on polycrystalline powder of **1** and **1F** under an applied magnetic field of 1000 Oe in the temperature range of 2−300 K. The temperature dependence of $\chi_M T$ for complex **1** and **1F** is depicted in Figure S51. The room temperature $\chi_M T$ values are found to be 10.78 cm^3 K mol^{-1} for **1** and 9.65 cm^3 K mol^{-1} for **1F**. These values are higher than that expected (7.5 cm^3 K mol^{-1}) for four noninteracting high-spin Co(II) ions (S = 3/2, g = 2.0). On decreasing the temperature, the $\chi_M T$ values gradually decrease and sharply fall to 0.97 and 0.34 cm^3 K mol^{-1} at 2.0 K for **1** and **1F**, respectively, indicating a singlet ground magnetic state (S_T = 0) with antiferromanetic exchange coupling between the high spin Co(II) ions. The data was modeled using the following spin Hamiltonian:

https://doi.org/10.1021/acscatal.2c05942
ACS Catal. 2023, 13, 8535−8550

$$\hat{H} = \sum_{i} \mu_B g \hat{S}_i \cdot H - 2J_{ij} \sum_{i,j;i\neq j} \hat{S}_i \cdot \hat{S}_j$$

with an isotropic g-value for each Co(II) center ($S = 3/2$), and isotropic magnetic exchange interaction J (six interactions between the four Co(II) ions lying on the vertices of a tetrahedron were considered). The best fit yields $g = 2.31$, $J = -1.16$ cm^{-1} for **1** and $g = 2.36$, $J = -2.46$ cm^{-1} for **1F**, respectively. The computational analysis of complex **1** and **1F** reveals similar exchange coupling values ($J = -2.34$ and -4.16 cm^{-1} for **1** and **1F**, respectively).

These computed values indicate a weak antiferromagnetic coupling, reinforcing the experimental observations. In case of **1**, the weak antiferromagnetic exchange can be attributed to the absence of any direct one-atom linker between the cobalt centers, while in **1F** the fluoride ion offers additional exchange pathway enabling marginally stronger antiferromagnetic exchange. Although single F^- bridge is expected to yield stronger antiferromagnetic coupling, trapping of the F^- ion inside the cubane restricts the Co−F−Co angle (≈108−109°), leading to a weak exchange interactions.[53,63]

Electrochemistry. The Co(II) clusters (**1**−**4**, **1F**−**4F**) provide the synergistic combination of precisely tuned electronic states and redox active metal centers to elicit significant interest for electrocatalytic water splitting. This is further aided by their chemical stability in ambient conditions while preserving their molecular discreteness and remaining insoluble in neutral aqueous media. This prompted the use of such precisely defined molecular systems as heterogeneous electrocatalysts for OER, HER and thereby overall water splitting (Figures 3a,b and S17). The chemical versatility

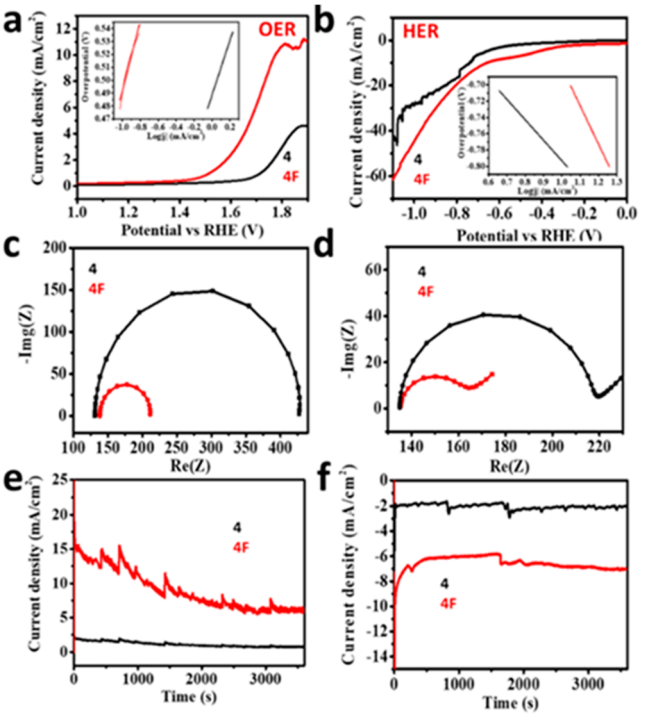

Figure 3. Linear sweep voltammograms (inset: Tafel slope) of **4** and **4F** for (a) OER and (b) HER in 1 M PBS electrolyte (pH = 7). Electrochemical impedance spectroscopy of **4** and **4F** for (c) HER and (d) OER. Chronoamperometry of **4** and **4F** for (e) HER and (f) OER. The spikes seen are due to evolution and delamination of gas bubbles.

enabled by the incorporation of fluorides and tuning of the exocubane two-electron donors provide a vast arena for a systematic exploration of these systems, leading to deeper fundamental understanding of the electronic effects associated with the water-splitting catalysis. As opposed to conventional molecular clusters such as Mn_4Ca and $Co(III)_4O_4$, which exhibit excellent activity toward either HER or OER, the quest has always been toward development of a single bifunctional molecular catalyst for overall water splitting.[40−42] The electrochemical studies elaborated herein unravel such hitherto unknown molecular bifunctional catalytic clusters that exhibit an unparalleled energy efficiency and kinetically facile catalytic activity for both HER and OER under near-neutral conditions.

The cubane clusters are directly immobilized on the surface of glassy-carbon electrode with loading ranging from 0.23 to 0.25 mg/cm^2. Notably, all the eight clusters tested were found to act as bifunctional catalysts for both HER and OER in near-neutral conditions (pH = 7.0), albeit to varying extents; a direct manifestation of the ligand-field effects and the associated electronic modulations. The observation of a prominent Co(II)/Co(III) redox couple (0.91 V vs RHE, Figure S18) in the cyclic voltammograms for all the eight clusters provides a robust fundamental basis of the OER proceeding via an oxo-bridge formation (Co(III)-OOH).[64] Furthermore, the signature of Co(III)/Co(IV) redox activity appearing at 1.24 V vs RHE uniformly across all the eight clusters confirms the formation of Co(III)-O$^\bullet$ as an intermediate in the HER.[65] Thus, all the eight clusters are capable of promoting both OER and HER and thus are, to our knowledge, the first set of molecularly assembled bifunctional catalysts for overall water splitting.

Catalysis by 1−4. The cluster **2** with pyridine as the exocubane ligand (Figure 1) exhibits an overpotential of 850 mV for HER and an onset potential of 630 mV for OER in near-neutral conditions. The corresponding values for cluster **1** that contains DMSO as the exocubane ligand (Figure 1) are 900 and 730 mV. While the electronic effects exerted by DMSO cannot be modified, attendant changes can be made on the pyridinic ligand by placing either electron-donating or electron-withdrawing substituents. Furthermore, electron-donating substituents may not have any positive effect on the catalysis, placing electron-withdrawing susbtituents such as $-NO_2$, −CHO, −CN can lead to depletion of charge-density at the cobalt center and thus facilitate coordination of water molecules to metal and trigger the electrocatalysis. Accordingly, formyl and cyano-substituted pyridines with increasing electron-withdrawing capabilities (**3** and **4**; Figure 1) were designed and evaluated for electrocatalysis. Consistent with the expectations, the distal functionalization on the para position of the pyridinic ring produces pronounced effect of HER and OER overpotentials for **3** and **4**. Specifically, the presence of a stronger electron withdrawing 4-cyano substituent on the pyridyl ring renders **4** as a superior catalyst compared to **3**. Effectively, these distal substitutents on the pyridine ligand modulates the positive charge on the metal. This is further substantiated by theoretical investigations which reveal that charge on cobalt center increases by 0.04 au for **4** vis-a-vis **1** (*vide infra*). The estimation of electrochemical onset overpotentials further confirms the above reasoning based on substituent effects, as can be seen through the order of kinetic facility for overall water splitting (**4**>**3**>**2**>**1**). This completely correlates to the anticipated inductive effects. Such ability to tune the catalytic activity through precise chemical function-

https://doi.org/10.1021/acscatal.2c05942
ACS Catal. 2023, 13, 8535−8550

alization is the first of its kind and opens up transformative pathways for rational chemical tailoring of heterogeneous catalysis.

The resulting order of onset overpotentials is in good agreement with the trends of interfacial charge-transfer resistance (R_{ct} of 300 Ω (HER) and 81.3 Ω (OER)) and the electrochemical double-layer capacitance (C_{dl} of 2.64 μF/cm^2 (HER) and 1.08 μF/cm^2 (HER)), values for **4** (Figure 3c, 3d, S21, Table S14). It can be discerned from Table S14 that **4** is the best catalyst among these four catalysts. The lower R_{ct} for **4** provides confirmatory evidence for facile charge-transfer through the active sites which in turn is driven by efficient and thermodynamically favored water coordination (*vide infra*). Similarly, the higher C_{dl} illustrates the crowding of water molecules around the electron-deficient Co(II) redox center, more so in case of electron-deficient **4**, and thus reduces any mass-transfer polarization effects.

*Catalysis by **1F**–**4F**.* In addition to the electronic modulations introduced by the distal functionalization, the presence of a central void in the cubane cage offers an attractive proposition for a more direct tuning of its electronic states. Accordingly, these clusters are rendered anionic through inclusion chemistry in an attempt to further improve the catalytic efficiency. Such an approach not only distorts the coordination symmetry of the cobalt from a pseudo-C_{3v} to an apparent-D_{3h}, but also further reduces the charge density on the metal thereby creating an ideal platform for facile water coordination (*vide infra*). Fluoride ion being the smallest of the anions (barring hydride) would be an ideal choice for the inclusion in the endocubane cavity.[66,67] Additionally, being the most electronegative element, it can further deplete the electron density from the cobalt centers to which it is equidistantly placed at ∼2.31 Å. Thus, it can be envisaged that oppositely directed electron drain by both fluoride and pyridine ligands would tend to serve the purpose of enhancing electrocatalytic efficiency. The change in the geometry around Co(II) also mimics a shuttle-relay mechanism, with a prominent effect on the kinetics of the electrocatalysis.

The synergistic effects of these processes result in **1F**–**4F** exhibiting significantly lower potentials than their corresponding nonfluorinated counterparts **1**–**4**. Such fluorinated cubanes also follow the same electronic order effected by the nature of L for overall water splitting (**4F**>**3F**>**2F**>**1F**, Figure 3a, b, Table 1 and S18). Of particular importance is the overpotential

Table 1. Cell Overpotential of the Catalysts under Neutral pH

Catalyst	Cell overpotential (V)	Catalyst	Cell overpotential (V)
1	1.63	**1F**	1.28
2	1.48	**2F**	1.05
3	1.33	**3F**	0.985
4	1.26	**4F**	0.949

of HER and onset potential of OER processes in case of **4F**, which reduces to 655 and 295 mV, respectively. Thus, the overall water splitting cell overpotential for **4F** is estimated to be 0.949 V.[68,69] This onset overpotential is also considerably lower than those reported for most solid-state materials, off-stoichiometric compounds and their combinations (Table S19). The redox peak assignments were carried out after evaluating the cyclic voltammograms at varying scan rates and ascribing them to Randles-Sevick analysis. The redox peak positions were also in agreement with those observed in literature for Co-based systems.[37,39,40,70,71] To the best of our knowledge, **4F** is the best performing heterogenized molecular electrocatalyst on an electrode surface (Figure 4, S19–S20).

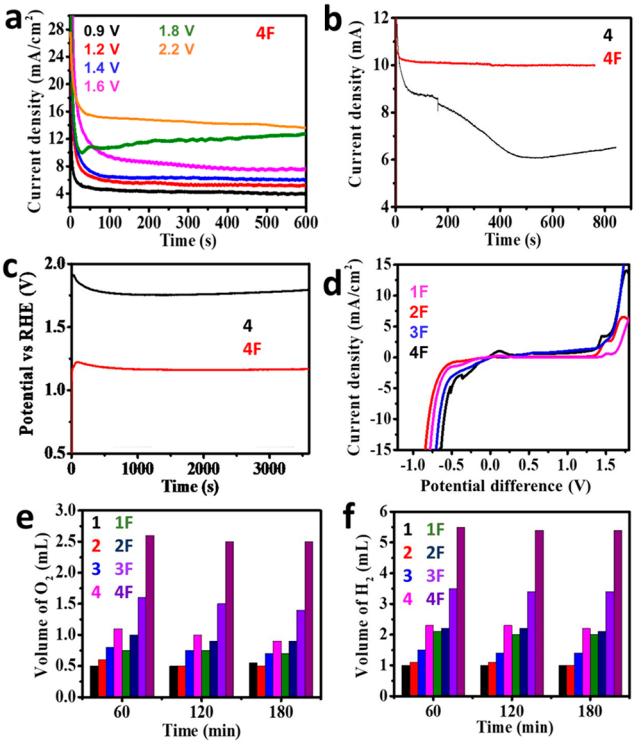

Figure 4. (a) Chronoamperometry of **4F** at different applied potentials for overall water splitting in 1 M PBS electrolyte. (b) Chronoamperometry of **4** and **4F** for overall water splitting in a two-electrode setup. The catalysts were drop-casted on carbon paper electrodes and ECSA estimated from Randles-Sevick plot. (c) Chronopotentiometry of **4** and **4F** for overall water splitting in a two-electrode setup (carbon paper as electrodes). (d) Linear sweep voltammograms of **1F**, **2F**, **3F**, and **4F** for overall water splitting. Quantification of (e) O_2 and (f) H_2 for all catalysts in a three-electrode setup.

The stability of **4F** catalyst was estimated by chronoamperometry at varying potentials (from 0.9 to 2.2 V) in a two-electrode setup (Figure 4). The catalyst **4F** exhibits stable current density of 10 mA/cm^2 under an applied potential of 2.2 V for over 1 h, with no detectable change (Figure 4a). The electrochemical stability of **4F** was evaluated by continued operation under chronopotentiometry (at 10 mA/cm^2, Figure 4c) and chronoamperometry (Figure 4b). Furthermore, the current density is amenable for facile enhancement, without affecting the operational stability as established by driving the **4F** system at 1.8 V to deliver a current density of 15 mA/cm^2 for over 1 h. In order to ascertain the electrochemical stability of **4F**, the cyclic voltammetry has been carried out for 30 cycles in 1 M PBS buffer (pH = 7.4). The redox activity corresponding to the $Co^{3+}\leftrightarrow Co^{4+}$ is distinct and invariant during these 30 cycles (Figure S19), confirming the electrochemical stability of the molecular heterogeneous catalysts. Similarly, the chronoamperometry has been performed for 10 h, and it has been found that the catalytic activity is not changed over the entire period (Figure S30).

https://doi.org/10.1021/acscatal.2c05942
ACS Catal. 2023, 13, 8535−8550

The bifunctionality of the catalyst is also demonstrated by overall linear sweep voltammograms (LSVs) and direct quantification of both H_2 and O_2 evolved during the process (Figure 4d−f). The overpotential and onset potential for both HER (655 mV) and OER (295 mV) is least for the cyano-substituent **4F** catalyst, providing the minimal cell overpotential (0.949 V, Figure 4d). These trends are also reflected in the hydrogen and oxygen generation (Figure 4e,f).

Extensive XPS studies provide useful insights to the mechanistic aspects of the catalysis apart from providing evidence for the stability of the catalysts during prolonged usage. All the molecular clusters (**1**−**4**, **1F**−**4F**) exhibit prominent peaks in X-ray photoelectron spectroscopy, arising due to the spin−orbit coupled Co(II) species (Figure S22−S25). The binding energy peaks at $2p_{3/2}$ and $2p_{1/2}$ observed at 781.2 and 797 eV for **1**, remains invariant for **1F**, in spite of change in coordination geometry. This is due to the balance of electron withdrawing endocubane substituent (fluoride) and the electron donating exocubane substituent (DMSO). In spite of this, both **1** and **1F** exhibit shakeup satellite peaks at 785.6 and 802.2 eV, with an energy difference of 15.8 eV confirming the presence of Co(II) in the as synthesized clusters. Further, the stability of the catalysts can be established by chronoamperometry for 10 h (Figure S30).

In contrast, the remaining molecular clusters (**2**−**4**, **2F**−**4F**) exhibit significant and systematic variations in the peak positions of Co(II). Distal substitution by an electron-withdrawing functionality results in the positive shift in binding energy to higher values. The magnitude of such shifts across **2** to **4** and **2F** to **4F**, are also in agreement with the electron-withdrawing ability of the -R group and thus follows the order **4** > **3** > **2** and **4F** > **3F** > **2F**. Thereby, the molecular cluster **4F** exhibits the highest binding energy of 781.7 and 804.5 eV, without compromising on the peak separation of 15.8 eV, reconfirming the Co(II) as the electroactive species.

The electron-deficiency on the Co(II), introduced by both endo- and exocubane functionalities are observed to produce a marked difference in their overall water splitting capabilities. The molecular cluster (**4F**) exhibiting the highest binding energy for Co(II) exhibits the lowest HER and OER onset overpotentials (655 and 295 mV, respectively). Although the cubanes investigated in this report exclusively contain Co(II), its atomic content is an important descriptor of the kinetic facility toward electrocatalysis (Figure 5a, Table S15). Importantly, the atomic content of Co(II) follows the exact order of their electrocatalytic performance and Tafel slope, with **4F** having the highest Co(II) content (25.6%) and lowest onset overpotential and Tafel slope (Figure S17, Table S13, as current density cannot reach up to 10 mA/cm^2, the onset overpotential has been calculated by extrapolating the tangent in LSV).[72,73] This provides critical information on the electron-deficient Co(II) as the active water coordination center for both HER and OER.

The electron-deficient Co(II) centers of cubane play an active role in water coordination. This is further reinforced through a quantitative estimation of the oxygen-deficiency in the molecular clusters. We would like to point out that the XPS spectra have been individually deconvoluted to estimate the proportion of oxygen that contributes to the water coordination. Therefore, while these numbers do not represent the molecular composition of the systems, it is a precise estimate of the role of oxygen and its availability for water coordination. Accordingly, cluster **4F** exhibits the highest

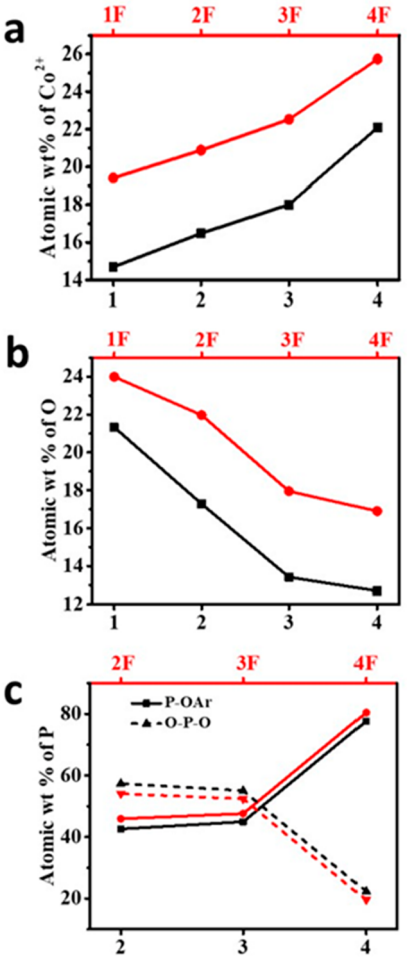

Figure 5. (a) Atomic% of Co(II), (b) atomic% of O, and (c) atomic% of P, calculated from XPS for the catalysts. Data collected from XPS spectra given in Figures S22−S25. The estimations provided here do not correspond to those obtained from survey spectrum, but to those derived from the deconvoluted high-resolution XPS spectra. Thus, the Co^{2+} from Co $2p_{3/2}$ (781 eV), P 2p (133 eV), originating from O−P−O and P−OAr (135 eV) and deconvoluted Co−O−P (532 eV) are taken into account to derive this plot.

oxygen deficiency (19.59%) among all the endocubane systems investigated (Figure 5b, S22−S25, Table S16), consistent with earlier observations. This enables the Co(II) center of **4F** to have the largest propensity toward coordinating the water molecules. Another feature directing the ability of these clusters to act as bifunctional catalysts is the presence of the phosphate moiety. While the electron deficient Co(II) drives the coordination of water leading to HER, the O−P−O bridging unit is critical for the OER process. Thus, a higher content of P−O−Ar in **4F** drives the subsequent OER process (Figures 5c, S22−S25, Table S17). This is in excellent agreement with the lowest bridging O−P−O content exhibited by **4F**. Thus, the synergism between a highly electron deficient Co(II) center, the endocubane-influenced geometrical distortion and the facile exposure of the phosphate moiety drive the coordination of water for both HER and OER processes.

The strong thermodynamic and kinetic dependence on the distal substitutions affords an unambiguous associative pathway leading to overall water-splitting. This is also in line with the change in the coordination geometry as observed in X-ray structure and Raman spectra (*vide supra*). The Raman

https://doi.org/10.1021/acscatal.2c05942
ACS Catal. 2023, 13, 8535−8550

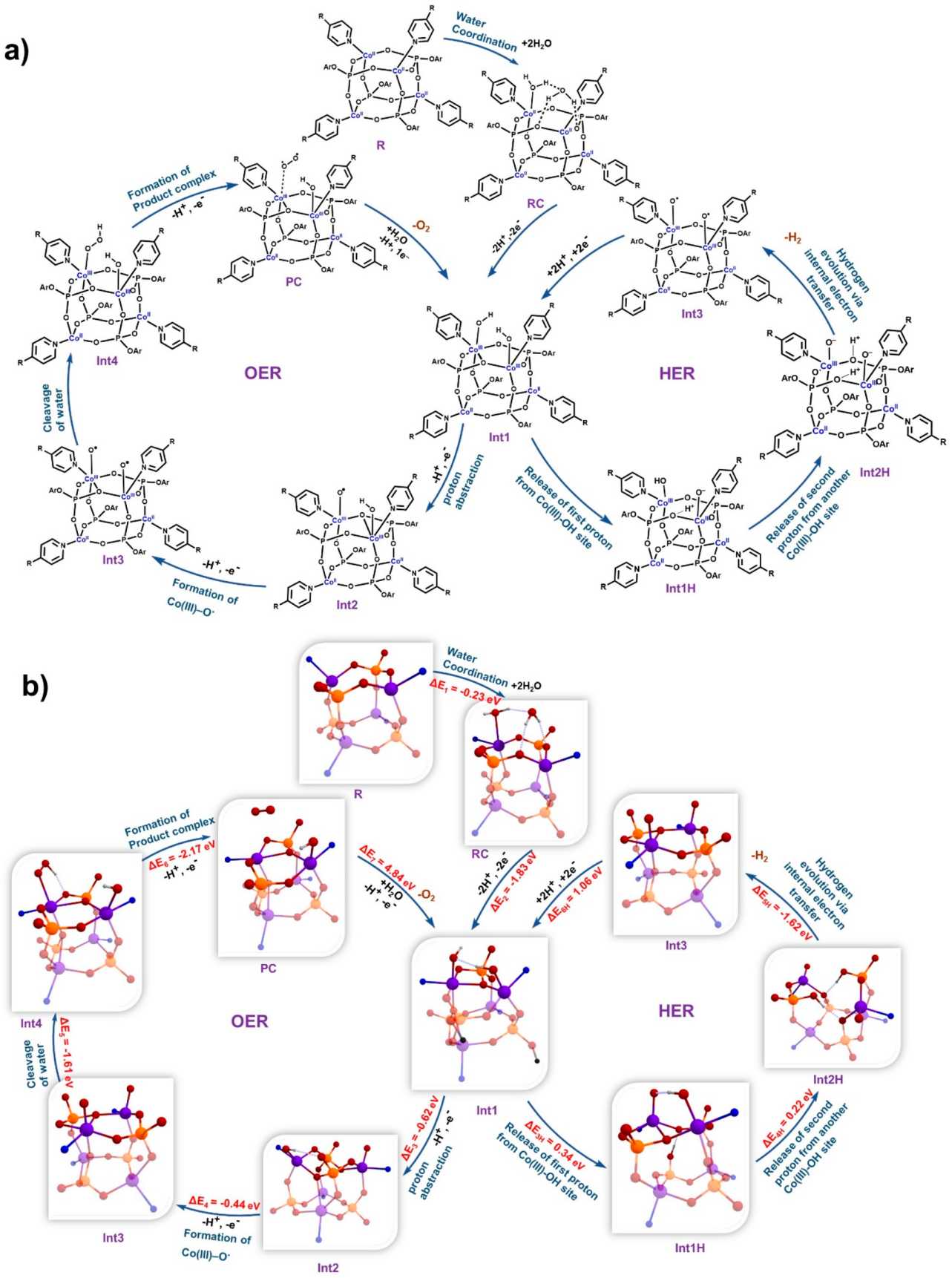

Figure 6. (a) Proposed mechanism for both OER and HER; (b) the catalytic cycles involved in both HER and OER in optimized **4** are shown as representative cases. Color code: violet-cobalt, red-oxygen, blue-nitrogen, orange-phosphorus, gray-carbon, and white-hydrogen.

https://doi.org/10.1021/acscatal.2c05942
ACS Catal. 2023, 13, 8535−8550

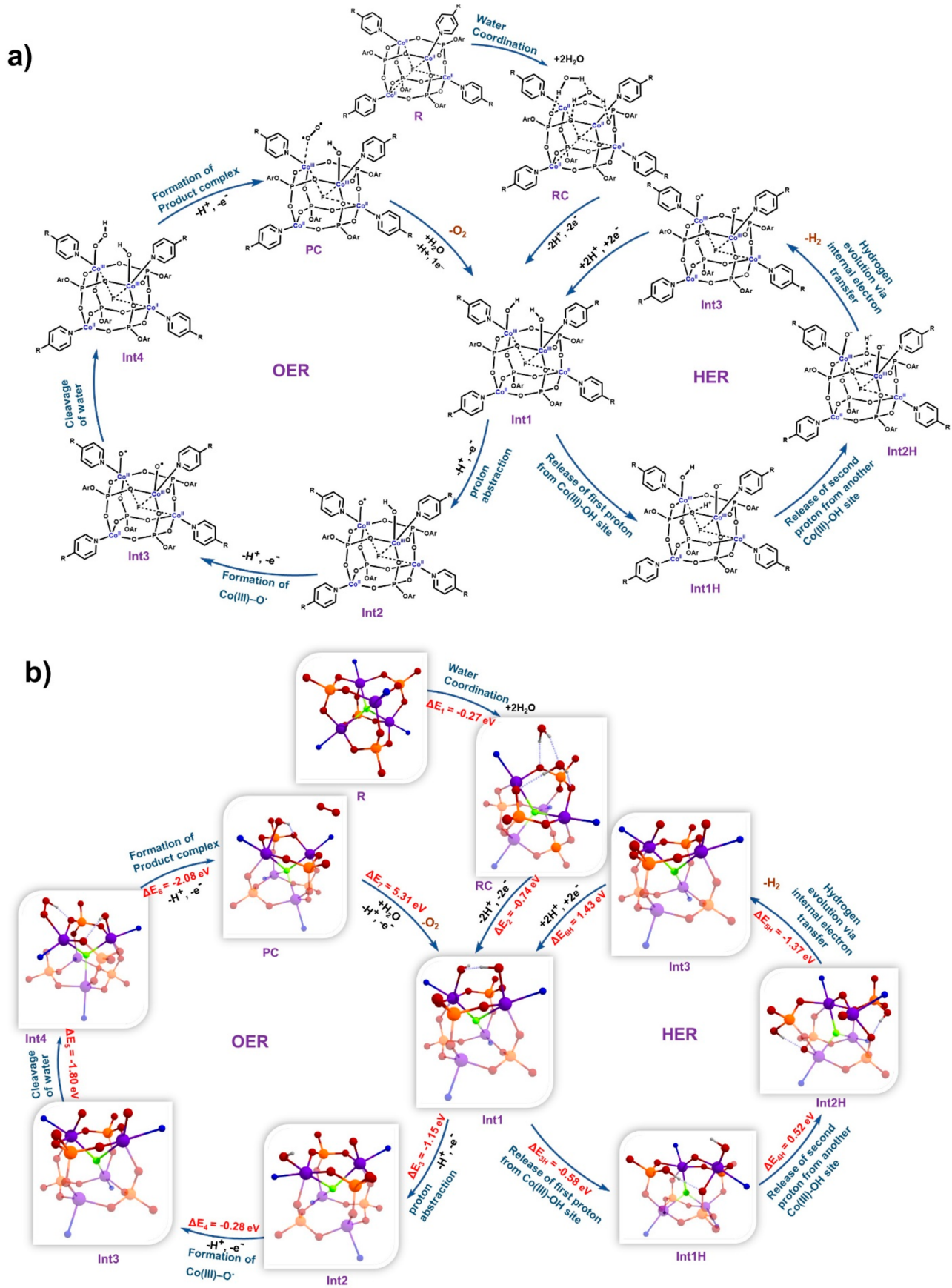

Figure 7. (a) Proposed catalytic mechanism for both OER and HER for **1F** − **4F**; (b) the catalytic cycles involved in both HER and OER in optimized **4F** are shown as representative cases. Color code: violet-cobalt, red- oxygen, blue-nitrogen, orange-phosphorus, green-fluorine, gray-carbon, and white-hydrogen.

https://doi.org/10.1021/acscatal.2c05942
ACS Catal. 2023, 13, 8535−8550

spectroscopy was performed before and after electrocatalysis to investigate the electronic changes occurs at the electrocatalytic centers (**2F**, **3F**, and **4F**). All the fluoride incorporated clusters **2F**−**4F** have been characterized by Raman spectroscopy. The characteristic peaks at 560 cm^{-1} (Co−O, F_{2g}) and 460 cm^{-1} (Co−O, E_{1g}), and 699 cm^{-1} (P−O), 1750 cm^{-1} (CHO), 1020 cm^{-1} (pyridine, **2**−**4** and **2F**−**4F**) and Co−F vibrational mode (420−440 cm^{-1}, **2F**−**4F**) are observed for all catalysts (Figure S31). Interestingly, minor shifts in the pyridinic peaks (1020 cm^{-1}) were observed signifying the direct involvement of the ligand environment in the charge transfer processes accompanying water splitting. The Co−F vibrational peak was observed to have a red shift, confirming the participation toward the electrochemical reaction. The strength of this Co−F vibrational mode was modified due to the coordination formed with the electrocatalytic Co center. Moreover, the clear retention of all the peaks indicates both the stability of the catalyst during the electrochemical process and the preservation of its integrity during the catalysis. Such chemical stability of **4** and **4F** is further confirmed by the means of powder X-ray diffraction studies. **4** and **4F** are soaked in water for a prolonged time (72 h) and the PXRD patterns obtained prior and subsequent to the soaking are found to be identical which confirms the phase purity and stability of the catalysts (Figures S47 and S48). Further, the postelectrocatalytic stabilities of the fluorinated clusters are supported by X-ray photoelectron spectroscopy. No significant shifts in XPS observed for C 1s, Co 2p, and O 1s peaks reflects the integrity of the oxidation states of the metal centers in the clusters. The increase in binding energy for C 1s and Co 2p observed due to the partial oxidation of the catalyst indicating the decrease in current density in chronoamperometry (Figures S26−S29).

Additional conclusive evidence was obtained from operando Raman spectro-electrochemical measurements carried out on the best performing catalyst (**4F**, Figure S32). A custom-made electrochemical cell consisting of a 3 cm aperture for spectroscopic measurement equipped with a bottom Indium-doped tin-oxide conductive glass (ITO, sheet resistance = 10 Ω sq^{-1}) acting as working electrode and Ag/AgCl, Pt wire serving as reference and counter electrode, respectively, was utilized for these measurements. Catalyst **4F** was spray-coated on the ITO and served as the working electrode. Onset of HER is accompanied by the emergence of peaks at 1600 cm^{-1} (cyanopyridine group), 1350 cm^{-1} (C−C), and 600 cm^{-1} (peroxide). Similarly, the OER is accompanied by enhancement of the vibrational modes corresponding to 1600 cm^{-1} (cyanopyridine group), 1350 cm^{-1} (C−C), and 550 cm^{-1} (peroxide). These vibrational modes that are spectroscopically tracked are also validated from DFT studies that indicate the bond vibrations at 604 cm^{-1} (hydroxide), 556 cm^{-1} (peroxide), and 1601−1657 cm^{-1} (all cyanopyridine group) in the intermediate species (^{15}**Int**$_4$).

Computational Studies. To understand the mechanistic insights into the catalytic bifunctionality of **4** and **4F**, DFT calculations were performed on **4** and **4F** to bring out the salient feature of fluoride incorporation and simultaneously investigate the mechanistic information resulting in low overpotentials for OER and HER (see computational details for the methodology employed).[74] Both **4** and **4F** consist of four Co(II) centers, albeit in tetrahedral or trigonal bipyramidal geometries, respectively. The phosphate bridges between the Co(II) centers enable exchange coupling between them. Besides, DFT optimization was carried out for **1**−**4** and **1F**−**4F** in order to extract their charges, spin densities and structural parameters (details in Figure S33 and Table S20−23). However, single-point energy calculations were performed for **4F** using its X-ray structure to ascertain the magnetic coupling using the established protocols.[75] The high symmetry around the Co(II) center in both **4** and **4F** dictates the existence of a single exchange coupling constant (J), as is computed to be −2.24 and −3.15 cm^{-1}, respectively.[76,77] Such low antiferromagnetic J values re-emphasize a diamagnetic ground state (S = 0) in these clusters (**1**−**4, 1F**−**4F**) and ensure close-lying exchange-coupled states that are easily accessible during overall water splitting.

Compared to the pristine clusters **1**−**4**, the endocubane clusters **1F**−**4F** exhibit longer Co−O, Co−N, and P−O bonds, consistent with the corresponding structural parameters obtained from X-ray diffraction, validating the computational methodology employed. In spite of the observed differences in the coordination geometry around Co(II) ion in complexes **4** and **4F**, both these complexes exhibit similar electronic configuration of $(d_{yz})^2(d_{xz})^2(d_{x^2-y^2})^1(d_{Z^2})^1(d_{xy})^1$, albeit changes in orbital energy ordering (see Figure S34, S35). A weak overlap of SOMOs (Singly Occupied Molecular Orbitals) of Co(II) centers via d_{xy} and $d_{x^2-y^2}$ orbital leads to a weak antiferromagnetic coupling for both **4** and **4F**. Furthermore, the presence of axial fluoride ion in **4F** produces a significant lowering of the absolute charge on the individual Co(II) centers by ∼0.1 au. This would, in turn, render the fluoride ion as the key player, both in generation and stabilization of higher oxidation states for cobalt during the catalysis, as has been elaborated vide infra.

To understand the possible pathways for enhanced water splitting efficiency of these complexes, the high-spin S = 6 state of both **4F** and **4** were investigated in detail. The mechanistic outcome that emanates from these calculations is pictorially represented in Figures 6 and 7, in which there are two catalytic cycles representing HER and OER. Considerable variations in terms of both the geometry and the oxidation states of Co(II) centers have been envisaged in these catalytic cycles, the energies of various spin states associated with the Co centers have also been investigated in detail. Attempts have also been made to compare the reactivity of one versus two metal centers for both complexes, **4** and **4F.**

The first catalytic step in both **4** and **4F** involves the attachment of a water molecule to either two Co(II) centers or a Co(II) center, both of which were computed with the former found to be energetically favorable (−0.45 and −0.48 eV). The exothermicity of this step for both **4** and **4F** (−0.23 and −0.27 eV, respectively) indicates an energetically favorable process. For **4** while one of the water molecules coordinate to the Co(II) center leading to a coordination expansion from trigonal bipyramidal, the second water molecule was found to have strong H-bonding interaction with the coordinated water molecule. For **4F**, on the other hand, both the water molecules are in the vicinity of the Co(II) center without a concrete metal−ligand bond as the geometry around Co(II) is already trigonal bipyramidal, and expansion to octahedral is likely to generate greater distortion. For **4**, the second water molecule is not only involved in H-bonding interaction with the coordinated H_2O (H···O distance of 1.764 Å) but also with the phosphate group of $\{Co_4O_4\}$ cubane (H···O(P) distance of 1.862 and 1.912 Å). For **4F**, on the other hand, as both the waters are not coordinated, they were found to have strong H-bonding interaction with each other (1.938 Å) and also with

https://doi.org/10.1021/acscatal.2c05942
ACS Catal. 2023, 13, 8535−8550

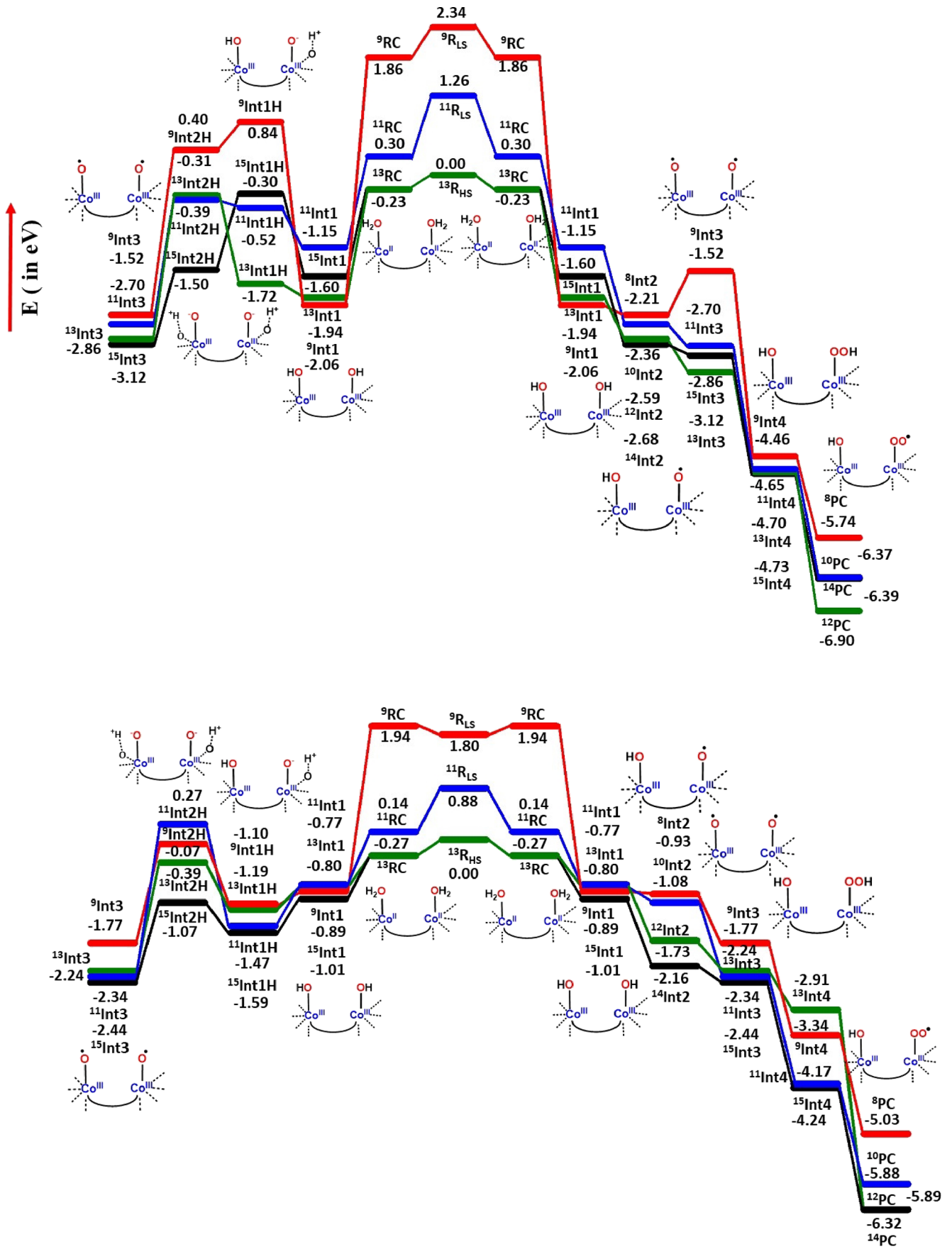

Figure 8. Potential energy profiles involved in catalysis by **4** and **4F** with appropriate intermediates.

https://doi.org/10.1021/acscatal.2c05942
ACS Catal. 2023, 13, 8535−8550

the phosphate group of the $\{Co_4O_4\}$ cubane (H···O(P) distance of 1.835 and 1.906 Å). These H-bonding interactions indicate that the water molecules are already activated.

In the next step of the HER and OER cycle, the formation of the putative Co(III)−OH species ((Intermediate 1; **Int1**) in both metal centers is assumed. The Co(III) center, thus generated, was found to alter the nature of spin-state from high-spin to other spin states such as low-spin or intermediate spin state for **4** while for **4F** the entire reaction was found to occur on the high-spin surface. The associated energetics for all the possible spin-states (S = 7, 6, 5 and 4) indicates that complex **4** has S = 4 as its ground state, which arises from S = 1 state for the dimeric $\{(Co(III)-OH)_2\}$ unit and the other two Co(II) centers having S = 3 which is maintained through the reaction. In the reactive $\{(Co(III)-OH)_2\}$ site, one square pyramidal Co(III) center possesses S = 1 state, and the other octahedral Co(III) center has S = 0 state due to bidentate coordination of the phosphate. For the **4F**, on the other hand, S = 7 is found to be the ground state, with each of the two Co(III) units possessing S = 2. The high-spin ground state observed for the Co(III) is essentially due to weaker Flouride binding, which also switches its nature of binding from μ_4 to μ_3 at this intermediate. This reveals that the presence of F^- ion has the ability to manure different spin-state and hence the reactivity.

Nevertheless, the S = 0 state of the Co(III) centers are only 0.12 eV higher (see Figure 8). At the S = 7 state, the Co(III)−OH species shows a strong delocalization of the spin density on the oxygen of the Co(III)−OH species (∼0.92), suggesting a strong radical character that is desired for the forthcoming steps. The formation of this intermediate is exothermic by −1.83 and −0.74 eV from the RC for **4** and **4F**, respectively (see computational details and Figures 6b and 7b). We have also performed the formation of Co(III)−OH species assuming the reactivity at a single Co(II) center, and this step is found to be less exothermic (−1.18 eV for **4F** and −1.32 eV for **4**, see the ESI). This emphasizes that a multinuclear cluster is important for water oxidation, and this is in line with other experiments where often multinuclear Co clusters were employed for the catalysts, with many examples reporting the absence of such reactivity for monomers.[78−80]

In the next step, formation of (Intermediate **2**; **Int2**) is assumed to take place via the release of one proton and an electron leading to the formation of the putative Co(III)-O$^\bullet$ species on one of the active centers with the other retaining the Co(III)−OH unit. Estimation of the energetics of all possible spin states on the Co(III)-O$^\bullet$ center (S = 13/2, 11/2, 9/2 and 7/2) establishes that this step is exothermic for both **4** and **4F** by −0.62 and −1.15 eV from **Int1**, respectively (see Figures 6b and 7b). Oxidation of Co(III)−OH to Co(III)-O$^\bullet$ results in stabilization of S = 3/2 centers resulting in the ground state of S = 13/2 for both **4F** and **4**, respectively. As the generation of putative Co(III)-O$^\bullet$ centers is challenging, the presence of strongly electronegative F^- ion help in such formation leading to greater exothermicity for **4F** compared to **4** in this step of the catalytic cycle. Careful analysis of the spin density plot of **Int2** reveals a significant oxyl radical character that suggests the formation of Co(III)-O$^\bullet$ species.[81] Employing a correlation developed based on multireference calculations on such electromeric species yield 14% of Co(III)-O$^\bullet$ character for **4** and 15% of Co(III)-O$^\bullet$ for **4F**, suggesting greater oxyl radical character for **4F** compared to **4**.[82] This is also reflected in the computed spin densities (0.96 vs 1.00). The role of Co(III)-O$^\bullet$ species oxidation of water in a homogeneous catalytic environment is highlighted recently also support our proposal.[81] The Co−O distance is estimated to be 1.627 and 1.611 Å in the case of complexes **4** and **4F**, respectively. Again, formation of such species computed at the single metal center was found to be exceedingly endothermic (2.12 eV for **4F** and 1.88 eV for **4**, see in ESI), while when both metals are involved, this was found to facilitate such oxidation by offering electronic cooperation.

Further in the OER cycle, **Int2** species loses one more proton as well as one electron to generate the aggressive dicobalt(IV)═O species (Intermediate 3; **Int3**) for the oxygen evolution process. The formation of this species is also found to be exothermic by −0.44 and −0.28 eV for complexes **4** and **4F**, respectively. The ground state for these two were observed to be S = 6 and S = 7, for **4** and **4F**, respectively. While all the putative Co(III)-O$^\bullet$ species exhibit a strong oxyl radical character, for **4F** one of the Co(III)-O$^\bullet$ species has high-spin S = 5/2 ground state suggesting a pure Co(III)-O$^\bullet$ character (Co−O bond length is 1.815 Å vs 1.609 Å). Strongly oxyl radical character has been attributed to greater reactivity in several high-valent oxo species earlier[37,71,83,84] and might be attributed to greater reactivity of **4F** observed in the experiments. In the successive step, the generation of aggressive Co(III)-O$^\bullet$ is therefore expected to activate the next water molecule via O···O bond formation, leading to the generation of Co(III)-OOH species (Intermediate **4**; **Int4**). The formation of this Co(III)-OOH species is further confirmed through in situ spectroelectrochemical Raman measurements with **4F**, further validating the computed mechanism (vide supra). Herein, the emergence of peak corresponding to Co(III)-OOH intermediate is clearly observed in the temporal evolution of the spectra, collected during the catalysis (Figure S32).

Formation of Co(III)-OOH species has also been found to be exothermic by −1.61 and −1.80 eV for **4** and **4F**, respectively,[85] (see Figure 6b and 7b) for S = 7 ground state with both Co(III) species possessing S = 2 ground state. As the O···O formation is the key step in the evolution of OER, we have also computed this step for a single Co center catalyst which is found to be exceedingly endothermic (+2.05 eV for **4** and +2.65 eV for **4F**, see in ESI). Addition of H$^\bullet$ and OH$^\bullet$ across dimeric Co(III)-O$^\bullet$ leading to the formation of Co(III)−OH and Co(III)-OOH species is found to be very favorable, suggesting strong cooperativity between two cobalt centers in the OER evolution again.

In the next step, hydrogen atom transfer from the Co(III)-OOH is assumed to take place and this results in the formation of O_2 and Co(II) species at the ground state and Co(III)-OO$^\bullet$ species at some excited spin states for both **4** and **4F** (see Figure 6b and 7b). This step is also found to be exothermic with respect to **Int4** by −2.08 eV for complex **4F** and −2.17 eV for complex **4**. It is important to note here that for **4F**, due to the presence of fluoride ion, the reactive metal centers maintain a high-spin state throughout the reaction and therefore, spin-crossover from one spin-state to the other is not necessary. For **4**, on the other hand, there are multiple spin-state crossovers detected during the course of the reaction. This spin-crossover with a lower oxidation state and weaker spin−orbit coupling results in larger energy penalties.[86−88] Despite favorable energetics in some of the steps involved, this spin state crossing is likely to hinder reactivity of

https://doi.org/10.1021/acscatal.2c05942
ACS Catal. 2023, 13, 8535−8550

4 compared to **4F**, and this is in agreement with experimental observations.

For the HER cycle, the Co(III)−OH species is the starting point of the catalytic cycle. Various pathways based experimental reports were attempted and this includes the formation of metal-hydride species and found that such mechanistic paths are energetically unfavorable for this reaction (See Table S24 in ESI). The mechanism for which favorable energetics are obtained is shown in Figures 6a and 7a. The first intermediate (**Int1H**) forms after the abstraction of a proton from the Co(III)−OH species by one of the phosphate oxygen atom leading to the formation of Co(III)-O^- species with $S = 6$ and $S = 7$ ground state for **4** and **4F**, respectively. The deprotonation of the Co(III)−OH species to Co(III)-Oxo species was achieved earlier in a tetrahedral ligand framework supporting this hypothesis.[89] These spin state differences arise due to the stabilization of high-spin Co(III) $S = 2$ on both metal centers in the case of **4F**, thanks to the presence of weak fluoride ion and formation of Co(III)−O-Co(III) species instead of a terminal Co(III)-O^- expected. For **4**, the Co(III)-O^- found to have $S = 2$ ground state with the Co(III)−OH having $S = 1$ as its ground state. The formation of this intermediate is found to be endothermic for **4** (0.34 eV) and exothermic for **4F** (−0.58 eV). A significant energy difference in this step suggests that the release of the proton is to be facilitated to a greater extent in the case of **4F**, compared to **4**, directly supporting the experimental observations. The next step is the formation of **Int2H**, which is formed upon the loss of another proton from the Co(III)−OH center. The formation of this species is found to be endothermic for both **4** (0.22 eV) and **4F** (0.52 eV) for the $S = 7$ state.

In the next step, the H_2 release is expected from two abstracted protons, which are in the phosphate arms along with $2e^-$ assumed to be released by the oxidation of metal ion from Co(III)-O^- to Co(III)-$O^\bullet$ (**Int3**).[90,91] The formation of this species is exothermic by −1.62 and −1.37 eV for complex **4** and **4F**, respectively. This is essentially due to the fact that these putative dicobalt(IV)═O species are in Co(III)-$O^\bullet$ species and, therefore, one-electron oxidation from Co(III)-O^- to Co(III)-$O^\bullet$ is favorable. In the HER cycle as well, several spin-state crossings were noted for **4**, while the entire reaction was found to occur in a high-spin surface for **4F**. This is again expected to facilitate faster H_2 release in **4F** compared to **4**.

If we compare the potential energy surface developed between OER and HER cycles, it is clear that in OER, all the intermediates formation are facile and exothermic, while in HER cycle, many steps are endothermic, and therefore, releasing H_2 is an energy-demanding slow process compared to OER. This observation is consistent with the experiments (See Figures 6, 7 and 8). Earlier observations that mononuclear complex do not split water (neither HER nor OER) and the recent report of two Co sites involvement in water splitting by Co_3O_4 augment our proposal, strongly supporting cooperativity in HER/OER reactivity.[78,92] Various potential intermediates for the HER mechanism, such as metal-hydride, Co(III)-$\bar{O}$ have been explored, but the energetic cost associated with the formation of such species are unfavorable (see Table S24, S61). Although the proposed species is a high-valent oxo species, the Mulliken charges computed reveal that the charges are decreasing on the metal center as we move along the species computed along the HER pathway, suggesting a favorable reaction under cathodic potential as observed in the experiments. Further, the internal hydrogen atom transfer that has been proposed here with organo-phosphate ligand is also supported by earlier studies on Cu(II) mediated HER reaction where phosphate ligands were found to be the proton acceptor and also another example of Zn(II) complex where N−H bonds in the ligands were found to facilitate the reaction,[93] offering confidence on the proposed mechanistic cycles from various perspective presented.[94]

CONCLUSIONS

We have demonstrated, in this contribution, a simple and straightforward strategy of ligand-field tuning on discrete tetranuclear Co(II) clusters to electronically manipulate the charge density on the redox-active metal center. This transforms the atom-precise cubane cage cluster to a bifunctional, heterogeneous catalyst for overall water splitting at an extremely competitive cell overpotential of 0.949 V. This study highlights the importance of systematic regulation of the charge density on the redox-active Co(II) center, for achieving kinetically enhanced water splitting activity, through two synergistic and tangential approaches: (a) introduction of an appropriate electron-withdrawing para-substituted pyridinic ligand, constituting exohedral ligand-field effect, and (b) endohedral encapsulation of fluoride anion that produces concomitant geometric and electronics effects. Cluster **4F**, representing the best combination of both these approaches, exhibits the lowest cell overpotential of 0.949 V among all known heterogeneous, molecular catalysts. Further, the DFT studies have unravelled the importance of cluster catalysis, where two phosphates and two Co(II) centers forming each face of the cubane clusters acts in tandem to provide the perfect environment for water coordination and subsequent HER and OER, respectively. A study of this sort, where suitably engineered molecular clusters can be rendered as heterogeneous catalysts opens up new avenues for overall electrochemical water splitting reactions. It is expected that these results will stimulate further interest in molecular cluster based heterogeneous catalysis, where the catalytically active metal ions such as cobalt and other transition metals will be placed in suitably chosen coordination environments for even better catalysis.

Although it has been possible to elucidate simultaneous OER and HER mechanisms of the parent (**1**−**4**) and fluorinated cubanes (**1F**−**4F**) through extensive computational studies described above, only a few of these proposed intermediates/key steps could be experimentally validated. This arises due to the complexity of the cluster systems and the presence of multiple reaction sites that cooperatively drive the overall water splitting. Given these limitations, currently it has not been possible to trap or characterize any further intermediates through in situ spectroscopic techniques. Thus, it would be prudent to further examine these complex systems through sized-down binuclear and mononuclear cobalt phosphate models. Work in this direction is currently underway in our laboratories.

ASSOCIATED CONTENT

Supporting Information

The Supporting Information is available free of charge at https://pubs.acs.org/doi/10.1021/acscatal.2c05942.

Additional figures and tables, crystallographic details, spectral characterization and computational details.

https://doi.org/10.1021/acscatal.2c05942
ACS Catal. 2023, 13, 8535−8550

Crystallographic information on the clusters. CCDC numbers 1983455, 1983456, 2008048, 2008049, 2008222, and 2008223 contain the supplementary crystallographic data for this paper. These data can be obtained free of charge from The Cambridge Crystallographic Data Centre. Optimized geometries of complexes **1**−**4**, and **1F**−**4F**, selected structural parameters, Mulliken charges and spin densities of reactant, intermediates and product complexes. Energy profile diagram and proposed schemes for both OER and HER cycle (PDF)

X-ray data for **1**, **1F**, **3F**, and **4F**(CIF)

X-ray data for **2** and **2F** (CIF)

Video of overall water splitting (MP4)

Water splitting video shot over 48 h (MOV)

AUTHOR INFORMATION

Corresponding Authors

Gopalan Rajaraman − *Department of Chemistry, Indian Institute of Technology Bombay, Mumbai 400076, India;* orcid.org/0000-0001-6133-3026; Email: rajaraman@chem.iitb.ac.in

Chandramouli Subramaniam − *Department of Chemistry, Indian Institute of Technology Bombay, Mumbai 400076, India;* orcid.org/0000-0001-8335-7395; Email: csubbu@chem.iitb.ac.in

Ramaswamy Murugavel − *Department of Chemistry, Indian Institute of Technology Bombay, Mumbai 400076, India;* orcid.org/0000-0002-1816-3225; Email: rmv@chem.iitb.ac.in

Authors

Aditya Borah − *Department of Chemistry, Indian Institute of Technology Bombay, Mumbai 400076, India*

Jayeeta Saha − *Department of Chemistry, Indian Institute of Technology Bombay, Mumbai 400076, India*

Sunita Sharma − *Department of Chemistry, Indian Institute of Technology Bombay, Mumbai 400076, India*

Savi Chaudhary − *Department of Chemistry, Indian Institute of Technology Bombay, Mumbai 400076, India*

Sandeep K. Gupta − *Department of Chemistry, Indian Institute of Technology Bombay, Mumbai 400076, India;* orcid.org/0000-0003-2432-933X

Complete contact information is available at: https://pubs.acs.org/10.1021/acscatal.2c05942

Author Contributions

†(J.S., S.S.) These authors contributed equally to this work.

Notes

The authors declare no competing financial interest.

ACKNOWLEDGMENTS

We thank SERB, New Delhi and Department of Science and Technology, Government of India for financial support (grants EMR/2017/002767 and SB/S2/JCB-85/2014 to R.M.; grants DST/TMD/MES/2k17/41 and SERB/F/9022/2019-2020 to C.S.; grants CRG/2018/000430; DST/SJF/CSA-03/2018-10; SB/SJF/2019-20/12 to G.R.). A.B. and S.S. would like to thank UGC, and J.S. would like to thank CSIR for research fellowships. The authors thank the central facilities at IIT Bombay for providing various characterization data.

DEDICATION

Dedicated to Professor Vadapalli Chandrasekhar on the occasion of his 65th Birthday

REFERENCES

(1) Yeo, B. S.; Bell, A. T. Enhanced activity of gold-supported cobalt oxide for the electrochemical evolution of oxygen. *J. Am. Chem. Soc.* **2011**, *133* (14), 5587−5593.

(2) Surendranath, Y.; Lutterman, D. A.; Liu, Y.; Nocera, D. G. Nucleation, growth, and repair of a cobalt-based oxygen evolving catalyst. *J. Am. Chem. Soc.* **2012**, *134* (14), 6326−6336.

(3) Ahn, H. S.; Tilley, T. D. Electrocatalytic water oxidation at neutral pH by a nanostructured $Co(PO_3)_2$ anode. *Adv. Funct. Mater.* **2013**, *23* (2), 227−233.

(4) Cabán-Acevedo, M.; Stone, M. L.; Schmidt, J.; Thomas, J. G.; Ding, Q.; Chang, H.-C.; Tsai, M.-L.; He, J.-H.; Jin, S. Efficient hydrogen evolution catalysis using ternary pyrite-type cobalt phosphosulphide. *Nat. Mater.* **2015**, *14* (12), 1245−1251.

(5) Wang, H.; Lee, H.-W.; Deng, Y.; Lu, Z.; Hsu, P.-C.; Liu, Y.; Lin, D.; Cui, Y. Bifunctional non-noble metal oxide nanoparticle electrocatalysts through lithium-induced conversion for overall water splitting. *Nat. Commun.* **2015**, *6* (1), 7261.

(6) Wang, J.; Cui, W.; Liu, Q.; Xing, Z.; Asiri, A. M.; Sun, X. Recent progress in cobalt-based heterogeneous catalysts for electrochemical water splitting. *Adv. Mater.* **2016**, *28* (2), 215−230.

(7) Zhou, H.; Yu, F.; Huang, Y.; Sun, J.; Zhu, Z.; Nielsen, R. J.; He, R.; Bao, J.; Goddard, W. A., III; Chen, S.; et al. Efficient hydrogen evolution by ternary molybdenum sulfoselenide particles on self-standing porous nickel diselenide foam. *Nat. Commun.* **2016**, *7* (1), 12765.

(8) Xue, Z. H.; Su, H.; Yu, Q. Y.; Zhang, B.; Wang, H. H.; Li, X. H.; Chen, J. S. Janus Co/CoP nanoparticles as efficient Mott-Schottky electrocatalysts for overall water splitting in wide pH range. *Adv. Energy Mater.* **2017**, *7* (12), 1602355.

(9) Hui, L.; Xue, Y.; Huang, B.; Yu, H.; Zhang, C.; Zhang, D.; Jia, D.; Zhao, Y.; Li, Y.; Liu, H.; et al. Overall water splitting by graphdiyne-exfoliated and-sandwiched layered double-hydroxide nanosheet arrays. *Nat. Commun.* **2018**, *9* (1), 5309.

(10) Park, J.; Kwon, T.; Kim, J.; Jin, H.; Kim, H. Y.; Kim, B.; Joo, S. H.; Lee, K. Hollow nanoparticles as emerging electrocatalysts for renewable energy conversion reactions. *Chem. Soc. Rev.* **2018**, *47* (22), 8173−8202.

(11) Wang, X.; Ma, W.; Ding, C.; Xu, Z.; Wang, H.; Zong, X.; Li, C. Amorphous multi-elements electrocatalysts with tunable bifunctionality toward overall water splitting. *ACS Catal.* **2018**, *8* (11), 9926−9935.

(12) Xu, H.; Cheng, D.; Cao, D.; Zeng, X. C. A universal principle for a rational design of single-atom electrocatalysts. *Nat. Catal.* **2018**, *1* (5), 339−348.

(13) Liu, Z.; Tan, H.; Liu, D.; Liu, X.; Xin, J.; Xie, J.; Zhao, M.; Song, L.; Dai, L.; Liu, H. Promotion of Overall Water Splitting Activity Over a Wide pH Range by Interfacial Electrical Effects of Metallic NiCo-nitrides Nanoparticle/NiCo2O4 Nanoflake/graphite Fibers. *Adv. Sci.* **2019**, *6* (5), 1801829.

(14) Sultan, S.; Ha, M.; Kim, D. Y.; Tiwari, J. N.; Myung, C. W.; Meena, A.; Shin, T. J.; Chae, K. H.; Kim, K. S. Superb water splitting activity of the electrocatalyst $Fe_3Co(PO_4)_4$ designed with computation aid. *Nat. Commun.* **2019**, *10* (1), 5195.

(15) Service, R. F. New electrolyzer splits water on the cheap. *Science* **2020**, *367* (6483), 1181−1181.

(16) Yan, Z.; Hitt, J. L.; Turner, J. A.; Mallouk, T. E. Renewable electricity storage using electrolysis. *Proc. Natl. Acad. Sci. U. S. A.* **2020**, *117* (23), 12558−12563.

(17) Oshima, T.; Nishioka, S.; Kikuchi, Y.; Hirai, S.; Yanagisawa, K.-i.; Eguchi, M.; Miseki, Y.; Yokoi, T.; Yui, T.; Kimoto, K.; et al. An Artificial Z-Scheme Constructed from Dye-Sensitized Metal Oxide Nanosheets for Visible Light-Driven Overall Water Splitting. *J. Am. Chem. Soc.* **2020**, *142* (18), 8412−8420.

(18) Anantharaj, S.; Noda, S. Amorphous catalysts and electrochemical water splitting: an untold story of harmony. *Small* **2020**, *16* (2), 1905779.
(19) Anantharaj, S.; Kundu, S.; Noda, S. The Fe Effect": A review unveiling the critical roles of Fe in enhancing OER activity of Ni and Co based catalysts. *Nano Energy* **2021**, *80*, 105514.
(20) Kanan, M. W.; Nocera, D. G. In situ formation of an oxygen-evolving catalyst in neutral water containing phosphate and Co^{2+}. *Science* **2008**, *321* (5892), 1072−1075.
(21) Smith, R. D.; Prévot, M. S.; Fagan, R. D.; Zhang, Z.; Sedach, P. A.; Siu, M. K. J.; Trudel, S.; Berlinguette, C. P. Photochemical route for accessing amorphous metal oxide materials for water oxidation catalysis. *Science* **2013**, *340* (6128), 60−63.
(22) Ullman, A. M.; Liu, Y.; Huynh, M.; Bediako, D. K.; Wang, H.; Anderson, B. L.; Powers, D. C.; Breen, J. J.; Abruña, H. c. D.; Nocera, D. G. Water oxidation catalysis by Co(II) impurities in $Co(III)_4O_4$ cubanes. *J. Am. Chem. Soc.* **2014**, *136* (50), 17681−17688.
(23) Yu, F.; Zhou, H.; Huang, Y.; Sun, J.; Qin, F.; Bao, J.; Goddard, W. A.; Chen, S.; Ren, Z. High-performance bifunctional porous non-noble metal phosphide catalyst for overall water splitting. *Nat. Commun.* **2018**, *9* (1), 2551.
(24) Han, X.; Ling, X.; Wang, Y.; Ma, T.; Zhong, C.; Hu, W.; Deng, Y. Spatial Isolation of Zeolitic Imidazole Frameworks-Derived Cobalt Catalysts: From Nanoparticle, Atomic Cluster to Single Atom. *Angew. Chem., Int. Ed.* **2019**, *58*, 5359.
(25) Yan, Z.; Zhu, L.; Li, Y. C.; Wycisk, R. J.; Pintauro, P. N.; Hickner, M. A.; Mallouk, T. E. The balance of electric field and interfacial catalysis in promoting water dissociation in bipolar membranes. *Energy Environ. Sci.* **2018**, *11* (8), 2235−2245.
(26) Lazouski, N.; Chung, M.; Williams, K.; Gala, M. L.; Manthiram, K. Non-aqueous gas diffusion electrodes for rapid ammonia synthesis from nitrogen and water-splitting-derived hydrogen. *Nat. Catal.* **2020**, *3* (5), 463−469.
(27) Yu, J.; Dai, Y.; He, Q.; Zhao, D.; Shao, Z.; Ni, M. A mini-review of noble-metal-free electrocatalysts for overall water splitting in non-alkaline electrolytes. *Mater. Today Energy* **2021**, *1* (2), 100024.
(28) Wang, M.; Zhang, L.; He, Y.; Zhu, H. Recent advances in transition-metal-sulfide-based bifunctional electrocatalysts for overall water splitting. *J. Mater. Chem. A* **2021**, *9* (9), 5320−5363.
(29) Tao, B. X.; Li, X. L.; Ye, C.; Zhang, Q.; Deng, Y. H.; Han, L.; Li, L. J.; Luo, H. Q.; Li, N. B. One-step hydrothermal synthesis of cobalt-vanadium based nanocomposites as bifunctional catalysts for overall water splitting. *Nanoscale* **2019**, *11* (39), 18238−18245.
(30) Wang, J.; Yue, X.; Yang, Y.; Sirisomboonchai, S.; Wang, P.; Ma, X.; Abudula, A.; Guan, G. Earth-abundant transition-metal-based bifunctional catalysts for overall electrochemical water splitting: A review. *J. Alloys Compd.* **2020**, *819*, 153346.
(31) Peng, J.; Dong, W.; Wang, Z.; Meng, Y.; Liu, W.; Song, P.; Liu, Z. Recent advances in 2D transition metal compounds for electrocatalytic full water splitting in neutral media. *Mater. Today Adv.* **2020**, *8*, 100081.
(32) Peng, X.; Jin, X.; Gao, B.; Liu, Z.; Chu, P. K. Strategies to improve cobalt-based electrocatalysts for electrochemical water splitting. *J. Catal.* **2021**, *398*, 54−66.
(33) Xu, Y.; Wang, C.; Huang, Y.; Fu, J. Recent advances in electrocatalysts for neutral and large-current-density water electrolysis. *Nano Energy* **2021**, *80*, 105545.
(34) Huang, C.; Qin, P.; Luo, Y.; Ruan, Q.; Liu, L.; Wu, Y.; Li, Q.; Xu, Y.; Liu, R.; Chu, P. K. Recent progress and perspective of cobalt-based catalysts for water splitting: design and nanoarchitectonics. *Mater. Today Energy* **2022**, *23*, 100911.
(35) Doan, T. L. L.; Nguyen, D. C.; Prabhakaran, S.; Kim, D. H.; Tran, D. T.; Kim, N. H.; Lee, J. H. Single-Atom Co-Decorated MoS2 Nanosheets Assembled on Metal Nitride Nanorod Arrays as an Efficient Bifunctional Electrocatalyst for pH-Universal Water Splitting. *Adv. Funct. Mater.* **2021**, *31* (26), 2100233.
(36) Surendranath, Y.; Kanan, M. W.; Nocera, D. G. Mechanistic studies of the oxygen evolution reaction by a cobalt-phosphate catalyst at neutral pH. *J. Am. Chem. Soc.* **2010**, *132* (46), 16501−16509.
(37) Nguyen, A. I.; Ziegler, M. S.; Oña-Burgos, P.; Sturzbecher-Hohne, M.; Kim, W.; Bellone, D. E.; Tilley, T. D. Mechanistic investigations of water oxidation by a molecular cobalt oxide analogue: Evidence for a highly oxidized intermediate and exclusive terminal oxo participation. *J. Am. Chem. Soc.* **2015**, *137* (40), 12865−12872.
(38) Nguyen, A. I.; Wang, J.; Levine, D. S.; Ziegler, M. S.; Tilley, T. D. Synthetic control and empirical prediction of redox potentials for Co_4O_4 cubanes over a 1.4 V range: Implications for catalyst design and evaluation of high-valent intermediates in water oxidation. *Chem. Sci.* **2017**, *8* (6), 4274−4284.
(39) Das, B. K.; Chakrabarty, R. Cobalt (III)-oxo cubane clusters as catalysts for oxidation of organic substrates. *J. Chem. Sci.* **2011**, *123* (2), 163−173.
(40) McCool, N. S.; Robinson, D. M.; Sheats, J. E.; Dismukes, G. C. A Co4O4 "cubane" water oxidation catalyst inspired by photosynthesis. *J. Am. Chem. Soc.* **2011**, *133* (30), 11446−11449.
(41) Brodsky, C. N.; Hadt, R. G.; Hayes, D.; Reinhart, B. J.; Li, N.; Chen, L. X.; Nocera, D. G. In situ characterization of cofacial Co(IV) centers in Co_4O_4 cubane: Modeling the high-valent active site in oxygen-evolving catalysts. *Proc. Natl. Acad. Sci. U. S. A.* **2017**, *114* (15), 3855−3860.
(42) Song, F.; Moré, R.; Schilling, M.; Smolentsev, G.; Azzaroli, N.; Fox, T.; Luber, S.; Patzke, G. R. $\{Co_4O_4\}$ and $\{Co_xNi_{4-x}O_4\}$ Cubane Water Oxidation Catalysts as Surface Cut-Outs of Cobalt Oxides. *J. Am. Chem. Soc.* **2017**, *139* (40), 14198−14208.
(43) Nguyen, A. I.; Van Allsburg, K. M.; Terban, M. W.; Bajdich, M.; Oktawiec, J.; Amtawong, J.; Ziegler, M. S.; Dombrowski, J. P.; Lakshmi, K.; Drisdell, W. S.; et al. Stabilization of reactive Co_4O_4 cubane oxygen-evolution catalysts within porous frameworks. *Proc. Natl. Acad. Sci. U. S. A.* **2019**, *116* (24), 11630−11639.
(44) Menezes, P. W.; Panda, C.; Walter, C.; Schwarze, M.; Driess, M. A cobalt-based amorphous bifunctional electrocatalysts for water-splitting evolved from a single-source lazulite cobalt phosphate. *Adv. Funct. Mater.* **2019**, *29* (32), 1808632.
(45) Murugavel, R.; Choudhury, A.; Walawalkar, M. G.; Pothiraja, R.; Rao, C. N. R. Metal complexes of organophosphate esters and open-framework metal phosphates: synthesis, structure, transformations, and applications. *Chem. Rev.* **2008**, *108* (9), 3549−3655.
(46) Murugavel, R.; Sathiyendiran, M.; Walawalkar, M. G. Di-tert-butyl Phosphate Complexes of Cobalt(II) and Zinc(II) as Precursors for Ceramic M(PO3)2 and M2P2O7Materials: Synthesis, Spectral Characterization, Structural Studies, and Role of Auxiliary Ligands. *Inorg. Chem.* **2001**, *40* (3), 427−434.
(47) Pothiraja, R.; Sathiyendiran, M.; Butcher, R. J.; Murugavel, R. Cobalt and Manganese Nets via Their Wires: Facile Transformation in Metal-Diorganophosphates. *Inorg. Chem.* **2004**, *43* (24), 7585−7587.
(48) Pothiraja, R.; Sathiyendiran, M.; Butcher, R. J.; Murugavel, R. Non-Interpenetrating Transition Metal Diorganophosphate 2-Dimensional Rectangular Grids from Their 1-Dimensional Wires: Structural Transformations under Mild Conditions. *Inorg. Chem.* **2005**, *44* (18), 6314−6323.
(49) Saha, J.; Verma, S.; Ball, R.; Subramaniam, C.; Murugavel, R. Compositional Control as the Key for Achieving Highly Efficient OER Electrocatalysis with Cobalt Phosphates Decorated Nanocarbon Florets. *Small* **2020**, *16*, 1903334.
(50) Murugavel, R.; Kuppuswamy, S. Octameric and Decameric Aluminophosphates. *Angew. Chem., Int. Ed.* **2006**, *45* (42), 7022−7026.
(51) Murugavel, R.; Kuppuswamy, S.; Boomishankar, R.; Steiner, A. Hierarchical Structures Built from a Molecular Zinc Phosphate Core. *Angew. Chem., Int. Ed.* **2006**, *45* (33), 5536−5540.
(52) Dar, A. A.; Sen, S.; Gupta, S. K.; Patwari, G. N.; Murugavel, R. Octanuclear zinc phosphates with hitherto unknown cluster architectures: ancillary ligand and solvent assisted structural transformations thereof. *Inorg. Chem.* **2015**, *54* (19), 9458−9469.

https://doi.org/10.1021/acscatal.2c05942
ACS Catal. 2023, 13, 8535−8550

(53) Gupta, S. K.; Dar, A. A.; Rajeshkumar, T.; Kuppuswamy, S.; Langley, S. K.; Murray, K. S.; Rajaraman, G.; Murugavel, R. Discrete $\{Gd^{III}{}_4M\}$(M= Gd^{III} or Co^{II}) pentanuclear complexes: a new class of metal-organophosphate molecular coolers. *Dalton Trans.* **2015**, *44* (13), 5961−5965.
(54) Gupta, S. K.; Kalita, A. C.; Dar, A. A.; Sen, S.; Patwari, G. N.; Murugavel, R. Elusive double-eight-ring zeolitic secondary building unit. *J. Am. Chem. Soc.* **2017**, *139* (1), 59−62.
(55) Sharma, K.; Gupta, S. K.; Borah, A.; Murugavel, R. Hitherto unknown eight-connected frameworks formed from $A_4B_4O_{12}$ metal organophosphate heterocubanes. *Chem. Commun.* **2019**, *55* (55), 7994−7997.
(56) Gupta, S. K.; Kuppuswamy, S.; Walsh, J. P.; McInnes, E. J.; Murugavel, R. Discrete and polymeric cobalt organophosphates: isolation of a 3-D cobalt phosphate framework exhibiting selective CO_2 capture. *Dalton Trans.* **2015**, *44* (12), 5587−5601.
(57) Mishra, A.; Wernsdorfer, W.; Abboud, K. A.; Christou, G. The first high oxidation state manganese-calcium cluster: relevance to the water oxidizing complex of photosynthesis. *Chem. Commun.* **2005**, No. 1, 54−56.
(58) Kalita, A. C.; Murugavel, R. Fluoride Ion Sensing and Caging by a Preformed Molecular D4R Zinc Phosphate Heterocubane. *Inorg. Chem.* **2014**, *53* (7), 3345−3353.
(59) Baerlocher, C.; McCusker, L. B.; Olson, D. H. Pnma. *Atlas of zeolite framework types*; Elsevier, 2007.
(60) Wilson, S. T.; Lok, B. M.; Messina, C. A.; Cannan, T. R.; Flanigen, E. M. Aluminophosphate molecular sieves: a new class of microporous crystalline inorganic solids. *J. Am. Chem. Soc.* **1982**, *104* (4), 1146−1147.
(61) Murugavel, R. Ceramic and porous framework metal silicates and phosphates from molecular precursors: an ever-evolving ambient synthesis approach. *Emergent Mater.* **2019**, *2*, 273.
(62) Bassindale, A. R.; Pourny, M.; Taylor, P. G.; Hursthouse, M. B.; Light, M. E. Fluoride-Ion Encapsulation within a Silsesquioxane Cage. *Angew. Chem., Int. Ed.* **2003**, *42* (30), 3488−3490.
(63) Langley, S. K.; Helliwell, M.; Teat, S. J.; Winpenny, R. E. P. Synthesis and characterisation of cobalt(ii) phosphonate cage complexes utilizing carboxylates and pyridonates as co-ligands. *Dalton Trans.* **2012**, *41* (41), 12807−12817.
(64) Wang, H.-Y.; Hung, S.-F.; Hsu, Y.-Y.; Zhang, L.; Miao, J.; Chan, T.-S.; Xiong, Q.; Liu, B. In situ spectroscopic identification of μ-OO bridging on spinel Co_3O_4 water oxidation electrocatalyst. *J. Phys. Chem. Lett.* **2016**, *7* (23), 4847−4853.
(65) Saha, J.; Ball, R.; Sah, A.; Kalyani, V.; Subramaniam, C. The mechanistic role of a support-catalyst interface in electrocatalytic water reduction by Co3O4 supported nanocarbon florets. *Nanoscale* **2019**, *11* (28), 13532−13540.
(66) Xue, Y.; Wang, Y.; Liu, H.; Yu, X.; Xue, H.; Feng, L. Electrochemical oxygen evolution reaction catalyzed by a novel nickel-cobalt-fluoride catalyst. *Chem. commun.* **2018**, *54* (48), 6204−6207.
(67) Kent, C. A.; Concepcion, J. J.; Dares, C. J.; Torelli, D. A.; Rieth, A. J.; Miller, A. S.; Hoertz, P. G.; Meyer, T. J. Water oxidation and oxygen monitoring by cobalt-modified fluorine-doped tin oxide electrodes. *J. Am. Chem. Soc.* **2013**, *135* (23), 8432−8435.
(68) Ng, J. W. D.; García-Melchor, M.; Bajdich, M.; Chakthranont, P.; Kirk, C.; Vojvodic, A.; Jaramillo, T. F. Gold-supported cerium-doped NiO_x catalysts for water oxidation. *Nat. Energy* **2016**, *1* (5), 16053.
(69) Cheng, N.; Stambula, S.; Wang, D.; Banis, M. N.; Liu, J.; Riese, A.; Xiao, B.; Li, R.; Sham, T.-K.; Liu, L.-M.; et al. Platinum single-atom and cluster catalysis of the hydrogen evolution reaction. *Nat. Commun.* **2016**, *7* (1), 13638.
(70) Sultan, S.; Ha, M.; Kim, D. Y.; Tiwari, J. N.; Myung, C. W.; Meena, A.; Shin, T. J.; Chae, K. H.; Kim, K. S. Superb water splitting activity of the electrocatalyst Fe3Co (PO4) 4 designed with computation aid. *Nat. Commun.* **2019**, *10* (1), 5195.
(71) Nguyen, A. I.; Wang, J.; Levine, D. S.; Ziegler, M. S.; Tilley, T. D. Synthetic control and empirical prediction of redox potentials for Co 4 O 4 cubanes over a 1.4 V range: Implications for catalyst design and evaluation of high-valent intermediates in water oxidation. *Chem. Sci.* **2017**, *8* (6), 4274−4284.
(72) Ahn, H. S.; Tilley, T. D. Electrocatalytic water oxidation at neutral pH by a nanostructured Co $(PO_3)_2$ anode. *Adv. Funct. Mater.* **2013**, *23* (2), 227−233.
(73) Saha, J.; Verma, S.; Ball, R.; Subramaniam, C.; Murugavel, R. Compositional Control as the Key for Achieving Highly Efficient OER Electrocatalysis with Cobalt Phosphates Decorated Nanocarbon Florets. *Small* **2020**, *16* (12), 1903334.
(74) Grimme, S.; Antony, J.; Ehrlich, S.; Krieg, H. A consistent and accurate ab initio parametrization of density functional dispersion correction (DFT-D) for the 94 elements H-Pu. *J. Chem. Phys.* **2010**, *132* (15), 154104.
(75) Noodleman, L. Valence bond description of antiferromagnetic coupling in transition metal dimers. *J. Chem. Phys.* **1981**, *74* (10), 5737−5743.
(76) Baskar, V.; Shanmugam, M.; Sañudo, E. C.; Shanmugam, M.; Collison, D.; McInnes, E. J.; Wei, Q.; Winpenny, R. E. Metal cages using a bulky phosphonate as a ligand. *Chem. Commun.* **2007**, No. 1, 37−39.
(77) Murugavel, R.; Shanmugan, S. Seeking tetrameric transition metal phosphonate with a D4R core and organising it into a 3-D supramolecular assembly. *Chem. Commun.* **2007**, No. 12, 1257−1259.
(78) Dey, A.; Kumar, V.; Pal, S.; Guha, A.; Bawari, S.; Narayanan, T. N.; Chandrasekhar, V. A tetranuclear cobalt (ii) phosphate possessing a D4R core: an efficient water oxidation catalyst. *Dalton Trans.* **2020**, *49* (15), 4878−4886.
(79) Okamura, M.; Kondo, M.; Kuga, R.; Kurashige, Y.; Yanai, T.; Hayami, S.; Praneeth, V. K.; Yoshida, M.; Yoneda, K.; Kawata, S.; et al. A pentanuclear iron catalyst designed for water oxidation. *Nature* **2016**, *530* (7591), 465−468.
(80) Ansari, A.; Ansari, M.; Singha, A.; Rajaraman, G. Interplay of Electronic Cooperativity and Exchange Coupling in Regulating the Reactivity of Diiron (IV)-oxo Complexes towards C- H and O- H Bond Activation. *Chem.—Eur. J.* **2017**, *23* (42), 10110−10125.
(81) Mondal, B.; Chattopadhyay, S.; Dey, S.; Mahammed, A.; Mittra, K.; Rana, A.; Gross, Z.; Dey, A. Elucidation of Factors That Govern the 2e-/2H+ vs 4e-/4H+ Selectivity of Water Oxidation by a Cobalt Corrole. *J. Am. Chem. Soc.* **2020**, *142* (50), 21040−21049.
(82) Sen, A.; Rajaraman, G. Can you break the oxo-wall? A multiconfigurational perspective. *Faraday Discuss.* **2022**, *234*, 175−194.
(83) Amtawong, J.; Nguyen, A. I.; Tilley, T. D. Mechanistic Aspects of Cobalt-Oxo Cubane Clusters in Oxidation Chemistry. *J. Am. Chem. Soc.* **2022**, *144* (4), 1475−1492.
(84) Ullman, A. M.; Brodsky, C. N.; Li, N.; Zheng, S.-L.; Nocera, D. G. Probing edge site reactivity of oxidic cobalt water oxidation catalysts. *J. Am. Chem. Soc.* **2016**, *138* (12), 4229−4236.
(85) McAlpin, J. G.; Surendranath, Y.; Dinca, M.; Stich, T. A.; Stoian, S. A.; Casey, W. H.; Nocera, D. G.; Britt, R. D. EPR evidence for Co (IV) species produced during water oxidation at neutral pH. *J. Am. Chem. Soc.* **2010**, *132* (20), 6882−6883.
(86) Yang, T.; Quesne, M. G.; Neu, H. M.; Cantú Reinhard, F. G.; Goldberg, D. P.; de Visser, S. P. Singlet versus triplet reactivity in an mn (v)-oxo species: testing theoretical predictions against experimental evidence. *J. Am. Chem. Soc.* **2016**, *138* (38), 12375−12386.
(87) Harvey, J. N.; Aschi, M.; Schwarz, H.; Koch, W. The singlet and triplet states of phenyl cation. *A hybrid approach for locating minimum energy crossing points between non-interacting potential energy surfaces. Theor. Chem. Acc.* **1998**, *99* (2), 95−99.
(88) Carreón-Macedo, J.-L.; Harvey, J. N. Do spin state changes matter in organometallic chemistry? A computational study. *J. Am. Chem. Soc.* **2004**, *126* (18), 5789−5797.
(89) Goetz, M. K.; Hill, E. A.; Filatov, A. S.; Anderson, J. S. Isolation of a terminal Co (III)-oxo complex. *J. Am. Chem. Soc.* **2018**, *140* (41), 13176−13180.

https://doi.org/10.1021/acscatal.2c05942
ACS Catal. 2023, 13, 8535−8550

(90) Karunadasa, H. I.; Chang, C. J.; Long, J. R. A molecular molybdenum-oxo catalyst for generating hydrogen from water. *Nature* **2010**, *464* (7293), 1329−1333.
(91) Yadav, P.; Nigel-Etinger, I.; Kumar, A.; Mizrahi, A.; Mahammed, A.; Fridman, N.; Lipstman, S.; Goldberg, I.; Gross, Z. Hydrogen evolution catalysis by terminal molybdenum-oxo complexes. *Iscience* **2021**, *24* (8), 102924.
(92) Curutchet, A.; Colinet, P.; Michel, C.; Steinmann, S. N.; Le Bahers, T. Two-sites are better than one: revisiting the OER mechanism on CoOOH by DFT with electrode polarization. *Phys. Chem. Chem. Phys.* **2020**, *22* (13), 7031−7038.
(93) Haddad, A. Z.; Garabato, B. D.; Kozlowski, P. M.; Buchanan, R. M.; Grapperhaus, C. A. Beyond metal-hydrides: non-transition-metal and metal-free ligand-centered electrocatalytic hydrogen evolution and hydrogen oxidation. *J. Am. Chem. Soc.* **2016**, *138* (25), 7844−7847.
(94) Coggins, M. K.; Zhang, M. T.; Chen, Z.; Song, N.; Meyer, T. J. Single-Site Copper (II) Water Oxidation Electrocatalysis: Rate Enhancements with HPO42- as a Proton Acceptor at pH 8. *Angew. Chem., Int. Ed.* **2014**, *53* (45), 12226−12230.

https://doi.org/10.1021/acscatal.2c05942
ACS Catal. 2023, 13, 8535−8550